Journal of Astronomical Telescopes, Instruments, and Systems

AstronomicalTelescopes.SPIEDigitalLibrary.org

Development of 13-μm cutoff HgCdTe detector arrays for astronomy

Mario S. Cabrera
Craig W. McMurtry
Meghan L. Dorn
William J. Forrest
Judith L. Pipher
Donald Lee

SPIE.

Mario S. Cabrera, Craig W. McMurtry, Meghan L. Dorn, William J. Forrest, Judith L. Pipher, Donald Lee, "Development of 13-μm cutoff HgCdTe detector arrays for astronomy," *J. Astron. Telesc. Instrum. Syst.* **5**(3), 036005 (2019), doi: 10.1117/1.JATIS.5.3.036005.

Development of 13-μm cutoff HgCdTe detector arrays for astronomy

Mario S. Cabrera,[a,*] Craig W. McMurtry,[a] Meghan L. Dorn,[a] William J. Forrest,[a] Judith L. Pipher,[a] and Donald Lee[b]
[a]University of Rochester, Department of Physics and Astronomy, Rochester, New York, United States
[b]Teledyne Imaging Systems, Camarillo, California, United States

Abstract. Building on the successful development of the 10-μm mercury cadmium telluride (HgCdTe) detector arrays for the proposed NEOCam mission, the University of Rochester Infrared Detector team and Teledyne Imaging Systems are working together to extend the cutoff wavelength of HgCdTe detector arrays initially to 13 μm, with the ultimate goal of developing 15-μm HgCdTe detector arrays for space and ground-based astronomy. The advantage of HgCdTe detector arrays is that they can operate at higher temperatures than the currently used arsenic doped silicon detector arrays at the longer wavelengths. Our infrared detector team at the University of Rochester has received and tested four 13-μm detector arrays from Teledyne Imaging Systems with three different pixel designs, two of which are meant to reduce quantum tunneling dark current. The pixel design of one of these arrays has mitigated the effects of quantum tunneling dark currents for which we have been able to achieve, at a temperature of 28 K and applied bias of 350 mV, a well depth of at least $75ke^-$ for 90% of the pixels with a median dark current of $1.8e^-/s$. These arrays have demonstrated encouraging results as we move forward to extending the cutoff wavelength to 15 μm. [DOI: 10.1117/1.JATIS.5.3.036005]

Keywords: infrared; detector; long wave infrared; mercury cadmium telluride; astronomy; space telescope.

Paper 18109 received Nov. 6, 2018; accepted for publication Aug. 9, 2019; published online Sep. 12, 2019.

1 Introduction

Cryogens or cryocoolers used to cool long-wave infrared (LWIR) detector arrays on space missions take up valuable space and weight, and the limited volume of cryogens limits the lifetime of the LWIR detector array sensitivity. This project addresses these limitations since the current ~13 μm (LW13), and eventual 15 μm (LW15) wavelength cutoff mercury cadmium telluride (HgCdTe) arrays can operate at temperatures that can be attained through passive cooling in space.

Instruments in past space missions that used LWIR detector arrays (wavelength cutoff above ~5 μm) required cooling to very low temperatures with on-board cryogens. For example, the Spitzer Space Telescope's Si:As impurity band conduction (IBC) LWIR arrays with a cutoff wavelength of ~28 μm used in all three instruments (IRAC, MIPC, and IRS)[1,2] were operated at 6 to 8 K, and the Wide-field Infrared Survey Explorer's (WISE) similar arrays (centered at 12 and 22 μm)[3] were cooled to 7.8 K. After cryogens ran out, due to good thermal design the focal plane of Spitzer Space Telescope warmed up and equilibrated to ~28 K. The mid-wave IR InSb cameras continue to function at comparable sensitivity to that during the cryogenic phase while the Si:As IBC LWIR large format detector arrays ceased to function due to high dark currents. Similarly, only the WISE mid-IR HgCdTe arrays continued to function once cryogen was depleted.

Figure 1 shows the median dark current versus temperature for all four ~13-μm cutoff wavelength HgCdTe arrays presented here, where three of the arrays show a median dark current $<1e^-/s$ at a temperature of 28 K and an applied bias of 150 mV.

Although the arrays presented here were developed for space missions, this technology can be important for ground-based observatories. Instruments developed to explore the N-band that use 13-μm HgCdTe arrays would be able to operate with the use of a cryo-cooler, eliminating the need for cryogens. We have initiated a study of this with colleagues, where our colleagues are experimenting with one of the LW13 arrays (H1RG-18508) to see if a fast readout (full-frame time of 12.5 ms) brings the N-band signal on scale, enabling astronomical observations with the array.

1.1 *Mercury Cadmium Telluride*

Our group and Teledyne Imaging Systems (TIS) are working together to develop new 15 μm LWIR detector arrays that can operate at relatively elevated focal plane temperatures for low background astronomy. TIS manufactures and develops these LWIR detector arrays with substantial feedback from our group. The testing and characterization of these devices is carried out at the University of Rochester (UR). The alloy used for these detectors, $Hg_{1-x}Cd_xTe$, has the x composition parameter (molar concentration of Cd) varied to reach different cutoff wavelengths. The band gap energy (in eV) of this semiconductor at a temperature in degrees Kelvin is given by[4]

$$E_g(x,T) = -0.302 + 1.93x - 0.81x^2 + 0.832x^3 + 5.35 \times 10^{-4}T(1-2x), \quad (1)$$

and the relationship between the band gap energy and the cut-off wavelength is given by

$$E_g = \frac{hc}{\lambda_c}, \quad (2)$$

where h is Planck's constant and c is the speed of light.

*Address all correspondence to Mario S. Cabrera, E-mail: mcabrer2@ur.rochester.edu

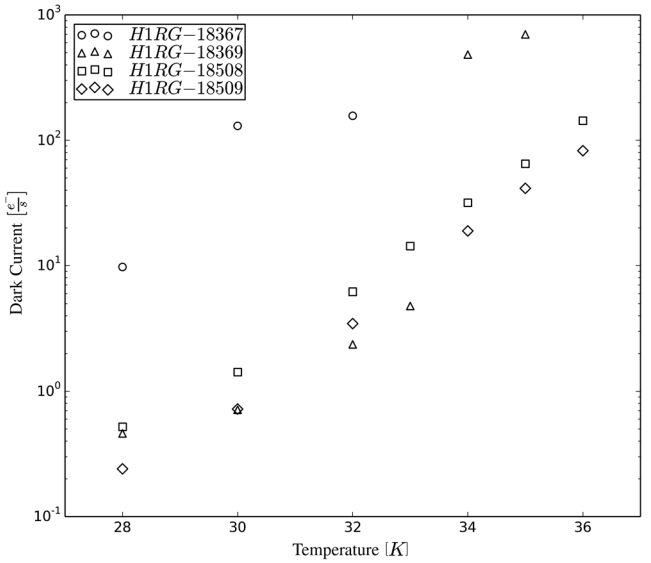

Fig. 1 Median dark current versus temperature with 150 mV of applied bias for all four ~13 μm cutoff wavelength arrays presented here. The dark current measurements for H1RG-18367 at all temperatures, and H1RG-18369 at 34 and 35 K were affected by a glow from the multiplexer, see Secs. 4.2 and 4.4.

1.2 *Prior Development/NEOCam*

The UR infrared detector team has been working on the development and improvement of low background devices with a cut-off wavelength longer than about 5.4 μm since 1992.[5–9] By 2003, these early large format arrays were 512×512 pixels and had cut-off wavelengths of 9.3 and 10.3 μm (LW10 arrays) and showed low dark current but could not support a large reverse bias, which limited the well depth of these devices. Even with these limitations, the devices showed promise as they were both operable at a temperature of 30 K.[6,10]

The Near Earth Object Camera (NEOCam) is a JPL proposed mission whose goal is to find and characterize near-Earth objects (asteroids and comets), some of which have Earth-crossing orbits and could be potentially hazardous. The mission will use the LW10 detector arrays discussed above to allow the telescope to observe from 6 to 10 μm. In addition to the instrumentation involving the LW10 arrays, NEOCam will also have a camera with lower cut-off wavelength arrays (5 μm) already developed for WISE and the James Webb Space Telescope.[11]

To meet the requirements of the NEOCam project, TIS successfully increased the array format from 512×512 to 2048×2048 pixels. The arrays have cut-off wavelengths of ~10 μm, low read noise, high quantum efficiency (QE), have operabilities (well depth of more than 44,000e^- and dark current less than 200e^-/s) > 90% up to temperatures of 42 K, and have been proton irradiated and demonstrated the ability to withstand the cosmic ray radiation that they are expected to receive in space.[12–14] These devices have reached NASA Technical Readiness Level-6.

1.3 *LW13 Detector Arrays*

In order to reach the present 15 μm goal (composition parameter $x \sim 0.209$, at a temperature of 30 K), we are completing an intermediate step by developing arrays with a cutoff wavelength of 13 μm ($x \sim 0.216$, at a temperature of 30 K) to identify any problems that would prevent us from reaching the 15 μm goal. As the compound becomes softer (which is a consequence of increasing the mercury fraction with increased wavelength), there is an increased likelihood of defects/dislocations[10] that would contribute to trap-assisted tunneling currents, as well as an increase in direct band-to-band tunneling due to the smaller band gap.[15–17]

Table 1 Cut-off wavelength and QE for all four LW13 arrays. QE values are expected to increase if arrays had antireflective coating.

Detector H1RG-	Wafer 2-	Lot-split	Cut-off wavelength (μm)	QE (6 to 10 μm)
18367	3757	Standard	12.8	74%
18508	3755	Standard	12.7	73%
18369	3763	Design 1	12.4	72%
18509	3759	Design 2	12.6	73%

We have received from TIS four 1024×1024 pixel arrays bonded to Hawaii-1RG multiplexers[18–20] with a pixel pitch of 18 μm and a wavelength cutoff of ~13 μm for the first phase of this project. Two of the four arrays, H1RG-18367 and H1RG-18508, were grown and processed in the same manner as the LW10 arrays for the proposed NEOCam mission, but extended to the desired 13 μm cutoff wavelength. Both H1RG-18369 and H1RG-18509 use TIS proprietary experimental structures designed to reduce tunneling dark currents, designated as design 1 and design 2, respectively.

TIS provided measurements of the QE before antireflection coating and cutoff wavelength from miniarrays on process evaluation chips (PECs) manufactured with the arrays, at a temperature of 30 K (Table 1). The QE as a function of wavelength was measured at UR using a circular variable filter, and we only quote the PEC QE measurements since we found a reasonable agreement with TIS measurements.

1.3.1 *Operability*

Operable pixels should have low initial dark current with sufficient well depth, high QE, and low read noise. The performance of the LW13 arrays has been shown to be limited by dark current and well depths during characterization.

These arrays have shown excellent QE (>70% before antireflection coating) and low correlated double sample (CDS) read noise (~23e^- shown for two arrays in Sec. 4.3) both at 30 K. We will show that high dark currents and/or low well depths limit the performance of these arrays. For this developmental project, we have focused our efforts in the reduction of high dark currents since their effects are expected to worsen when the wavelength is increased to the final goal of 15 μm. Therefore, pixels with low dark current and sufficient well depth will be considered operable.

We adopt the same dark current operablity requirements to that of the LW10 devices developed for the NEOCam mission.[14] Our imposed operability requirements include dark currents <200e^-/s and well depth of ~40ke^- for an applied bias of 150 mV (larger well depth requirements are used for larger applied biases). The dark current requirement for NEOCam was established such that the mission's 6 to 10 μm channel will be

background-limited by the thermal emission from the zodiacal dust cloud.

The operability requirements adopted for NEOCam are also specific to the filters, telescope size, and throughput. Any future mission that intends to use these LW13 devices likely would have a modified set of requirements.

Though operability requirements depend on specific applications of these devices, the dark current and well depth requirements for operable pixels in the LW13 arrays are used as a benchmark to compare the performance of the different arrays at different temperatures and applied bias and to determine the best pixel design that will be pursued when increasing the cutoff wavelength to 15 μm.

1.3.2 *Sources of dark current and their implications*

Thermal (diffusion[21] and generation-recombination[22]) and tunneling (band-to-band and trap-to-band) dark currents have been found to be the sources of dark current in these LW13 devices. Tunneling currents are the primary dark current mechanisms limiting the operability of the LW13 arrays at low temperatures and moderate high applied reverse bias required for use with low-power source-follower readout integrated circuit commonly used for astronomy focal plane arrays.

Both tunneling dark currents are strong functions of bias and have large nonlinear effects that can affect data calibration. In addition to the nonlinear effects, the charge capacity of pixels with very large dark currents, due to trap-to-band tunneling, can be depleted leading to low well depths, where a subset of these pixels creates a cross-hatching pattern in the operability map for all four arrays (see Sec. 4.4.1).

The design of H1RG-18509 successfully lowered tunneling dark currents, where the median dark current and well depth at a temperature of 28 K and reverse applied bias of 350 mV is $1.8e^-/\mathrm{s}$ and $81ke^-$, respectively, while the median dark current for the other three arrays was $>200e^-/\mathrm{s}$. The effects of tunneling currents on calibration and operability for all four devices are shown in Sec. 4.

The dark current of these devices has been modeled using the theory described in the following section. The results are shown in Sec. 5, where we have shown that at biases $> \sim 200$ mV and low temperatures, band-to-band tunneling is the dominant component of dark current and is shown to be fairly uniform since all pixels are affected equally by this dark current mechanism.

Operating regimes in which thermal currents dominate would be ideal to avoid any nonlinear dark current behavior as pixels debias due to integrating signal since both diffusion and generation-recombination dark currents do not vary significantly with a bias above 25 mV. These regimes will be further discussed in Sec. 6.

2 Dark Current Theory

2.1 *Diffusion Current*

Diffusion dark current occurs when electrons in the valence band gain enough energy thermally to overcome the band gap and transition to the conduction band. This thermally induced current must occur within one diffusion length (much larger than the pixel width and depth in these arrays) from the depletion region and is given by[21]

$$I_{\mathrm{dif}} = A\frac{n_i^2 d}{N_d \tau_b}\left[\exp\left(\frac{qV_{\text{actual bias}}}{k_b T}\right) - 1\right], \tag{3}$$

where A is the diode junction area, n_i is the intrinsic carrier concentration, d is the thickness of the n-type region, N_d is the doping density, τ_b is the minority carrier (hole in the n-type region) lifetime, k_b is Boltzmann's constant, and T is the temperature. In reverse bias, the actual bias across the diode ($V_{\text{actual bias}}$) is negative and the exponential term is negligible for the applied biases that we typically apply (>25 mV of reverse bias). It can be readily seen that diffusion dark current does not change appreciably with varying bias while the strong temperature dependence comes in the form of the intrinsic carrier concentration[4]

$$n_i = (5.585 - 3.820x + 1.753\times 10^{-3}T - 1.364\times 10^{-3}xT) \times\left[10^{14}E_g^{3/4}T^{3/2}\exp\left(-\frac{E_g}{2k_bT}\right)\right], \tag{4}$$

where x is the cadmium mole fraction.

2.2 *Generation-Recombination*

The second source of dark current that increases with temperature is generation-recombination (G-R). Traps in the depletion region with energy levels between the valence band and the conduction band can facilitate the indirect transition of an electron to the conduction band, where electrons in traps would have to overcome a smaller energy gap. G-R current is given in Ref. 22 by

$$I_{\text{G-R}} = \frac{n_i W_D A}{\tau_{\mathrm{GR}}}\left[\frac{\sinh\left(\frac{-qV_{\text{actual}}}{2kT}\right)}{\frac{q(V_{\text{bi}}-V_{\text{actual}})}{2kT}}\right] f(b), \tag{5}$$

$$f(b) = \int_0^\infty \frac{dz}{z^2 + 2bz + 1}, \tag{6}$$

$$b = \exp\left[\frac{-qV_{\text{actual}}}{2kT}\right]\cosh\left(\frac{E_i - E_{t_{\mathrm{gr}}}}{kT}\right). \tag{7}$$

$E_{t_{\mathrm{gr}}}$ is the trap energy level position with respect to the valence band, which contributes the most to the G-R current, E_i is the intrinsic Fermi level ($E_g/2$). τ_{GR} is the depletion region lifetime for holes and electrons, and W_D is the depletion region width given by[5]

$$W_D = \sqrt{\frac{2\epsilon\epsilon_0(V_{\text{bi}} - V_{\text{actual bias}})}{qN_d}}, \tag{8}$$

where ϵ_0 is the permittivity of free space, ϵ is the relative permittivity of HgCdTe, and V_{bi} is the built-in voltage. G-R current also has a very weak dependence on bias (as long as the back-bias is greater than ~25 mV).

2.3 *Quantum Tunneling Currents*

Tunneling currents are produced by electrons tunneling from the valence to the conduction band directly (band-to-band) or by traps with energies between the valence and the conduction band (trap-to-band). There are two different models for band-to-band currents; the first assumes a triangular barrier, whereas the

second one uses a parabolic barrier. The equation corresponding to the parabolic barrier is omitted here as our data best match the behavior of a triangular barrier, and it is given by[15,16]

$$I_{\text{band-to-band}} = -\frac{q^2 A E V_{\text{actual bias}}}{4\pi^2\hbar^2}\sqrt{\frac{2m_{\text{eff}}}{E_g}}\exp\left(-\frac{4\sqrt{2m_{\text{eff}}}E_g^{3/2}}{3q\hbar E}\right), \tag{9}$$

where m_{eff} is the effective mass of the minority carrier and E is the electric field across the depletion region given by[21]

$$E = \sqrt{\frac{2N_d(E_g - qV_{\text{actual bias}})}{\epsilon\epsilon_0}}. \tag{10}$$

Trap-to-band tunneling current for a triangular barrier is modeled as[15,17]

$$I_{\text{trap-to-band}} = \frac{\pi^2 q m_{\text{eff}} A V_{\text{actual bias}} M^2 n_t}{h^3(E_g - E_t)} \times \exp\left[-\frac{4\sqrt{2m_{\text{eff}}}(E_g - E_t)^{3/2}}{3qE\hbar}\right], \tag{11}$$

where M is the mass matrix, E_t is the energy of the trap level with respect to the valence band, and n_t is the trap density in the depletion region at E_t.

Data from pixels that appear to exhibit trap-to-band tunneling in the LW10[5,8,9] and the LW13 devices have also shown a soft breakdown in the *I–V* curves, prior to the onset of trap-to-band tunneling. Other authors have observed soft breakdowns in 4H-SiC[23,24] and silicon[25] diodes caused by screw dislocations and stacking faults, respectively, which became electrically active at a certain "threshold voltage." Furthermore, Neudeck et al.,[23] Ravi et al.,[25] and Benson et al.[26] (for HgCdTe on Si) showed that there is no correlation between the degraded *I-V* characteristics and the trap density, because all traps associated with dislocations may not contribute to the soft breakdown due to the varying threshold voltage for dislocations within the same diode at which they become electrically active.

Though we cannot say with certainty what type of dislocation[10] causes the soft breakdown in the LW13 arrays presented here, we believe a defect associated mechanism, likely different from that described by the authors above is responsible for this early soft breakdown and the onset of trap-to-band tunneling as traps become electrically active. Bacon[8] parametrically fit the *I-V* curves by introducing a threshold voltage at which certain traps become active and contribute to trap-to-band tunneling as

$$n_t = n_{t_i} + \frac{n_{t_d}}{1 + \exp\left[\frac{\gamma q(V_a + V_{\text{actual bias}})}{kT}\right]}, \tag{12}$$

where n_{t_i} is an initial active trap density, n_{t_d} is the trap density due to activated dislocations at a voltage V_a, and γ is a parameter that dictates how sharply the current increases due to the soft breakdown before reaching the current expected from trap-to-band tunneling. A small modification to Eq. (2.29) in Ref. 8 was made where we multiply the sum of the activation voltage and the actual bias by γ. This change was made so that the fitted γ parameter only affected the sharpness of the soft breakdown and not the fitted activation voltage.

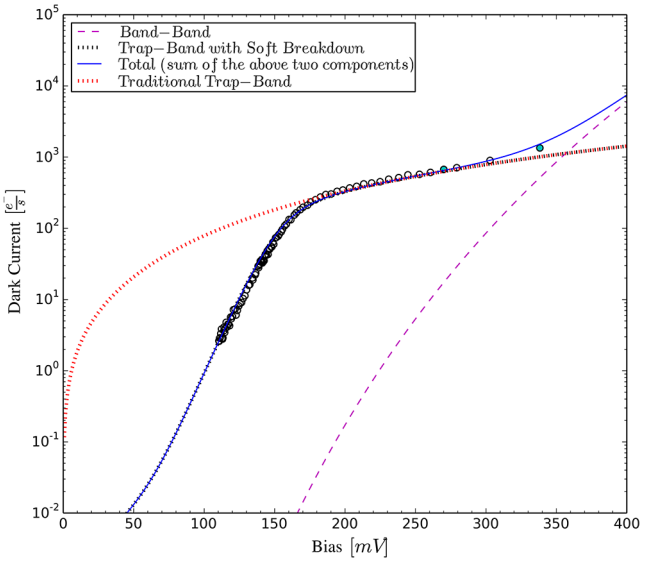

Fig. 2 Dark current versus bias at a temperature of 28 K for an inoperable pixel in H1RG-18369. Trap-to-band tunneling with a constant trap density and with variable trap density (due to activated traps) are plotted for comparison. The total curve corresponds to the sum of band-to-band and trap-to-band with soft breakdown curves.

Although this is not a physical model since we do not know the trap identity, a more detailed study using this phenomenological fit can give us information about the traps such as the trap density and a distribution of trap energies.

Figure 2 shows the *I-V* data (see Sec. 5.2 for a description of how *I-V* data are obtained) of an inoperable pixel that can be modeled with trap-to-band tunneling following the soft breakdown. Below 170 mV of applied reverse bias, trap-to-band tunneling with the assumption of a constant trap density at all biases (labeled as "traditional trap-band") does not fit the data, requiring the use of Eq. (12), which allows for the activation of traps. Similar behavior can be seen among inoperable pixels in all four LW13 arrays, where the data following the soft breakdown can be modeled by trap-to-band tunneling.

More data at lower biases would be needed to more accurately characterize the threshold voltage of the traps that contribute to the trap-to-band tunneling, whereas data at larger biases are needed to properly characterize pixels that only appear to show the soft break down, and there is no indication if the behavior before or after the soft breakdown is consistent with trap-to-band tunneling or any other form of dark current.

3 Data Acquisition

UR uses a liquid helium dewar with multiple chambers to test the arrays. The innermost chamber that houses the array and filter wheel has an aluminum cylindrical shield coupled to a liquid helium reservoir, allowing temperatures down to 4 K and below (by reducing the pressure in the liquid helium reservoir) to be reached. The filter wheel has several narrow band filters, two circular variable filters (covering a wavelength range between 4 and 14.3 μm), and a dark blocking filter. Attached to the filter wheel housing is a 67.6-μm diameter Lyot stop used to control the illumination of the array. The temperature inside the innermost chamber is regulated with a Lake Shore

Cryotronics temperature controller, allowing the arrays presented here to be tested at different stable temperatures.

The inner chamber is surrounded by an aluminum cylindrical shield attached to a liquid nitrogen reservoir, shielding the liquid helium reservoir and inner chamber from the outer shell, which is at room temperature. The outer shell has an antireflection-coated ZnSe window in the line of sight of the array being tested.

The array controller used for data acquisition is based on an open source hardware design developed by the Observatory of the Carnegie Institute of Washington (OCIW). The version that we use is optimized for infrared arrays. It has programmable clocks and biases with four channels of amplification and analog-to-digital conversion for the output of the array. A detailed description of the array controller can be found in Ref. 27.

3.1 *Sampling Modes*

The data presented here were obtained using either the sample-up-the-ramp (SUTR) or Correlated Double Sample (CDS or Fowler-1) sampling methods,[28–30] where the method used for specific data sets will be mentioned in their description. The same reset mode is used for both sampling methods, where a reverse bias (V_{bias}) is applied to reset the array row by row (all columns in a row simultaneously). Immediately after the reset switch is turned off to allow the device to debias as signal and dark current are accumulated, a redistribution of charge (pedestal injection due to capacitive coupling to the reset FET) results in a change in the bias voltage across the diode to a value designated as V_{actual}.

Following the reset, the first sampled image is referred to as the pedestal. The delay time to the pedestal sample ranges from circa 5.8 ms to 5.8 s, depending on the row and column for a specific pixel. For CDS images, the pedestal is subtracted from an image sampled some integration time later. The SUTR method is used to obtain many nondestructive samples to study the behavior of the array as pixels debias over time. In this sampling mode, following the reset and pedestal frame (used to normalize the rest of the samples to a zero point), many samples are taken at equal time intervals without resetting the array.

4 Characterization

To characterize the performance of the LW13 arrays, we measured the dark current and well depth (amount of charge collected at the integrating node when saturation is reached) per pixel at temperatures ranging from 28 to 36 K with applied reverse bias of 150, 250, and 350 mV, as well as the read-noise per pixel at a temperature of 30 K for two of the arrays. The node capacitance and signal linearity have also been measured at a temperature of 30 K with applied reverse bias of 150, 250, and 350 mV to calibrate the arrays.

4.1 *Calibration*

The first step in the calibration process is to measure the source-follower FET gain of signal in the multiplexer by turning on the reset switch and varying the reset voltage while recording the output voltage. The source-follower FET gain was measured to be ~0.9 for all four arrays, allowing us to convert between the output referred and input referred signal.

Next, to convert from volts to electrons, we measure the nodal capacitance. Our data are recorded in analog to digital units (ADU), which can be converted to volts by dividing the 5 V range of the 16 bit A/D converter by 2^{16} ADUs and the gain from our array controller electronics. The nodal capacitance per pixel is obtained using the noise squared (σ^2) versus signal method[31] shown in Fig. 3. Sets of 100 CDS images, each set at varying fluence levels, were used to obtain the signal and the rms noise. Figure 4 shows the nodal capacitance distribution per pixel for H1RG-18508 for three applied biases, where the median capacitance is then used to convert between the measured ADUs and the signal in electrons for the entire array.

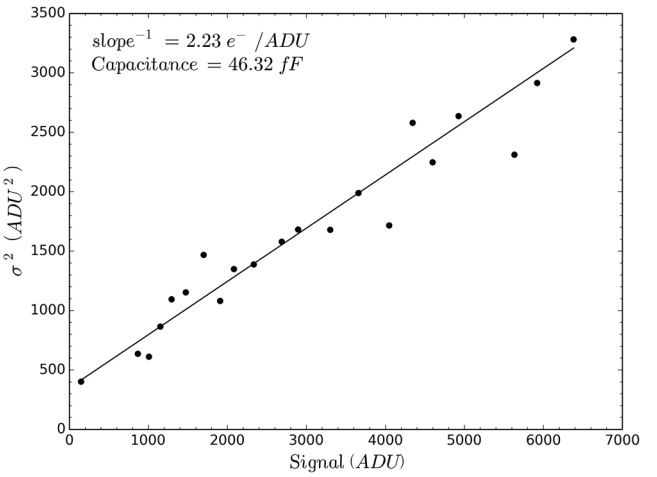

Fig. 3 Noise squared versus signal plot for a pixel in H1RG-18508 at a temperature of 30 K and 150 mV of applied bias, where the slope of the fitted line corresponds to the conversion factor between ADUs and e^-. The capacitance calculated here is not yet corrected for IPC.

The capacitance then has to be corrected for interpixel capacitance (IPC), determined through the nearest neighbor method. Pixels with a very high signal (due to very high dark currents) are used to determine the coupling parameter α between the high signal pixel and its nearest neighbors.[32] The nodal capacitance is then multiplied by a factor of $1 - 8\alpha$ to correct for IPC.[32] The IPC coupling factor α and corrected capacitance for all four arrays are shown in Table 2 for three applied biases.

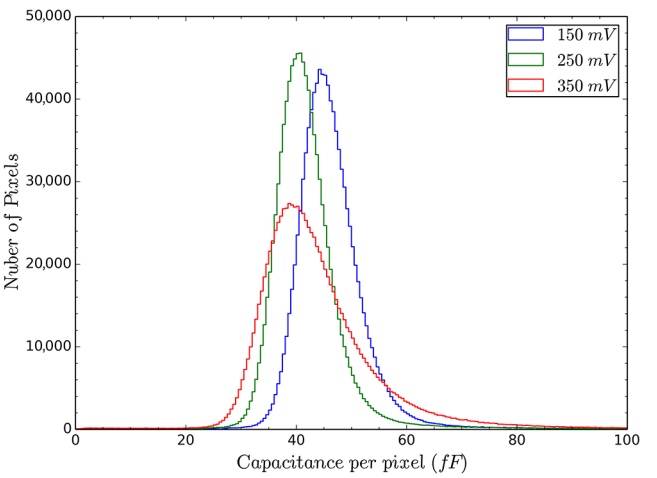

Fig. 4 Capacitance per pixel distribution for H1RG-18508 at a temperature of 30 K and at all tested applied biases. These capacitances have not yet been corrected for IPC. The spread in the capacitance distribution is due to noise. One standard deviation away from the mean for the 150 and 250 mV distributions is equal to 6.8 and 10.5 fF for the 350-mV distribution.

Table 2 IPC coupling parameter α is given for each of the arrays, as well as the median IPC corrected capacitance in femtofarads for each of the applied biases.

		150 mV	250 mV	350 mV
Detector H1RG-	α (%)	Median capacitance (fF) corrected for IPC		
18367	1.04	43	37	35
18508	1.03	42	38	38
18369	1.04	38	36	35
18509	1.12	39	37	34

This method of converting the signal at the integrating node to electrons is only valid for low signal data that minimize debiasing as in Fig. 3. For large signals, we need to account for the nonlinear diode capacitance resulting from the debiasing of the diode, leading to the reduction of the junction depletion region as signal is collected.[33] To measure the nonlinearity of these devices, the signal collected from a constant illuminating flux is sampled in SUTR mode until saturation is reached. The nonlinear collected signal rate is calculated by dividing the signal over the time it took to collect the signal. The signal is not corrected for dark current.

Figure 5 shows the nonlinearity curve for H1RG-18509 with an applied bias of 150 mV at 30 K, normalized to the first sampled signal. The normalized signal rate is also referred to as C_0/C, where C_0 is the nodal capacitance at zero collected signal and C is the nodal capacitance. To correct for the nonlinear capacitance, the slope of a fitted line to the nonlinearity curve (between 20% and 80% of the saturating signal) is used.

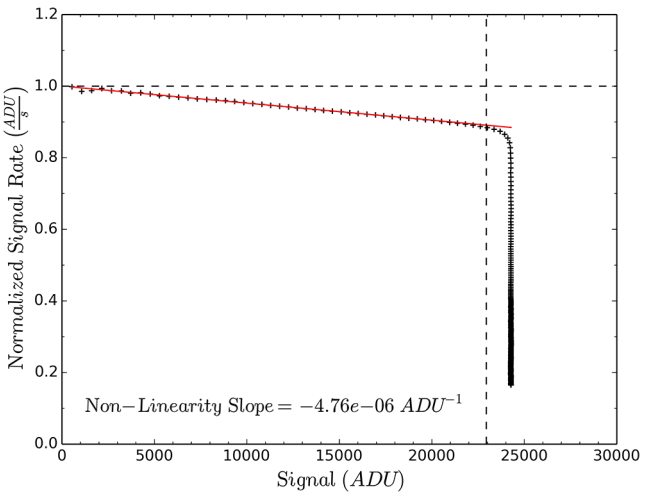

Fig. 5 Nonlinearity curve obtained from a 50 × 50 box average of pixels in H1RG-18509 with an applied bias of 150 mV at a temperature of 30 K. The collected signal rate was normalized to that corresponding to the lowest signal. The difference between a value of unity (horizontal dashed line) and the nonlinearity curve is the fraction of the signal not collected due to the debiasing of the device. The vertical dashed line corresponds to the mean saturating signal (well depth) for the entire device, which occurs at actual zero bias. The saturation of the nonlinearity curve occurs at a higher signal value due to the forward biasing of the detector by the signal flux used to saturate the array.

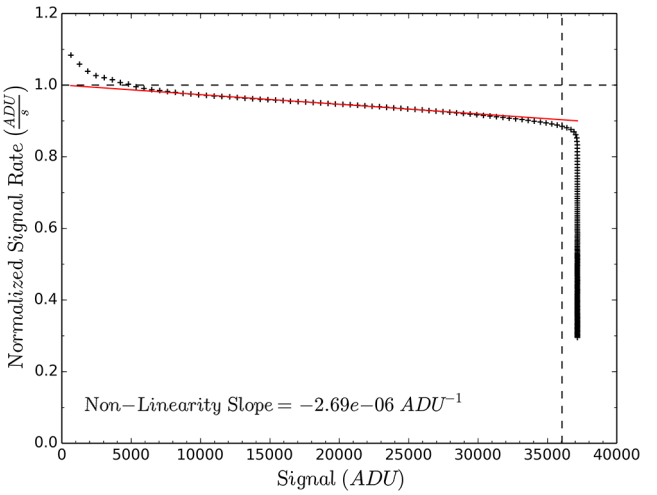

Fig. 6 Nonlinearity curve obtained from a 50 × 50 box average of pixels in H1RG-18369 with an applied bias of 250 mV at a temperature of 30 K. The signal rate was normalized and shifted such that the fitted line has a *y*-intercept of unity. The difference between a value of unity (horizontal dashed line) and the nonlinearity curve is the fraction of the signal that was not collected due to the debiasing of the device. The vertical dashed line corresponds to the mean saturating signal at an actual bias of zero for the entire device. The rapid debiasing of the detector at low signals is due to tunneling dark currents.

Correcting for the nonlinearity can be difficult when dark currents are on the order of the collected signal, which can occur at biases larger than 150 mV. A further step is required at high bias, where the extrapolated line fit is normalized to unity at zero signal.

Figure 6 shows the nonlinearity curve for H1RG-18369 with an applied bias of 250 mV, where at low signals the rate at which the diode debiases is much faster than is expected from a constant flux illumination. This quick debiasing is due to elevated dark current levels at high bias attributed to quantum mechanical tunneling. The effects of tunneling dark currents that are dominant at larger bias are further discussed in Secs. 4.4 and 5.

4.2 *Mux Glow*

In multiple occasions during the characterization of H1RG-18367 and H1RG-18369, a uniform elevated current was measured when taking data in the dark. This elevated current affected dark current at 150 mV (34 and 35 K), 250 mV (33-35 K), and read noise at 30 K and 150 mV of applied bias for H1RG-18369. All of the dark current measurements for H1RG-18367 were affected by this elevated current.

A light leak in the test dewar has been ruled out because the anomalous dark current was not present in all data sets taken under similar conditions (without changes to the system setup). Figure 20 shows an instance where an elevated current affected the dark current and well depth data but was not present in the warm-up data (discussed in Sec. 5.1) taken at a similar temperature and same applied bias. Dark current has also been ruled out since the dark current mechanisms studied here do not increase by a factor of 10 or more by increasing the temperature by 1 K for H1RG-18367 and -18369 (see Fig. 1 or Tables 4 and 8). Instead, we believe this current could be a glow from the unit cell FETs in the multiplexer. This effect will be referred to as "mux glow" hereafter when describing the data that were

affected. Further work is required to evaluate this anomalous behavior.

4.3 *CDS Read Noise*

The total noise per pixel was measured for two arrays, H1RG-18369 and H1RG-18509 at a temperature of 30 K and an applied bias of 150 mV. To compute the read noise, 64 SUTR sets (each SUTR consisting of 36 samples) were taken in the dark with an integration time of 5.5 s between each sample. From this, 64 Fowler-1 (CDS) images were created, where the total rms noise was calculated. The total CDS noise when measured in the dark is expected to be dominated by the read noise.

Shot noise from an elevated current measured for H1RG-18369 in this data set, most likely due to a "mux glow," is subtracted in quadrature from the total CDS noise to obtain the CDS read noise. The current per pixel is calculated by fitting a line to each of the 64 SUTR curves taken in the dark, where the mean of the 64 fitted slopes is the current.

The mean dark current for H1RG-18509 was measured to be $0.8e^-/s$, whereas the elevated current for H1RG-18369 was $80e^-/s$, compared to the $0.7e^-/s$ measured in the data set taken to determine the dark current and well depth at the same temperature and bias (discussed in Sec. 4.4).

Figure 7 shows the distribution of rms read noise per pixel for both arrays, where the median noise is $22.9e^-$ and $23.2e^-$ for H1RG-18369 and H1RG-18509, respectively. The majority of pixels with low noise approximately between 10 and $15e^-$ in the read noise distribution for H1RG-18509 and in the total noise distribution for H1RG-18369 are located in the "picture frame" region[34] of the arrays.

4.4 *Dark Current and Well Depth (Operability)*

To measure the dark current and well depth, 200 samples-up-the-ramp in the dark were taken with an integration time of 5.8 s between each sample. Without resetting, we allow a radiative flux to uniformly saturate the array, where this saturating level includes a 10 to 20 mV forward bias contribution from the signal flux.[8] To determine the actual zero bias saturation signal for each pixel, the array is then read out 200 additional times in the dark, allowing the array to debias to actual zero bias. The initial dark current is the measured slope at the beginning of the signal versus time (SUTR) curve. The difference between the pedestal frame and the average of the last 20 frames (taken when the array is at zero bias) then gives us the well depth of each pixel.

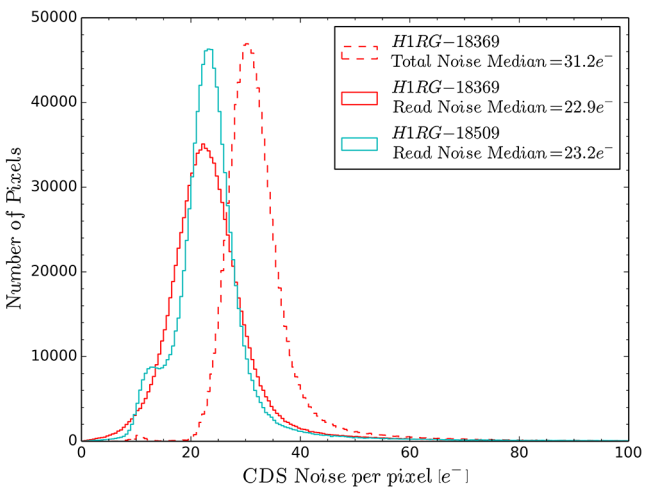

Fig. 7 Histogram of CDS read noise per pixel for H1RG-18369 and H1RG-18509 at a temperature of 30 K and applied bias of 150 mV. The total noise is plotted for H1RG-18369 to show the contribution from the "mux glow" to the noise of the detector. The dark current contribution from H1RG-18509 to the total noise was minimal and did not exhibit a "mux glow."

Well depth and dark current are presented here concurrently because the initial dark current of a pixel may be heavily dependent on the actual bias (well depth) across the pixel when it is first sampled (referred to as pedestal). Quantum tunneling dark currents are exponentially dependent on bias, so large tunneling dark currents can debias a pixel considerably between reset and pedestal frame, thus showing a low initial dark current but with a depleted well.

4.4.1 *H1RG-18367*

Figure 8 shows the distribution of initial dark current versus well depth per pixel for H1RG-18367 at a temperature of 28 K and applied bias of 150 mV, where the operable pixels are below and to the right of the dashed lines. The dark current distribution per pixel for this array peaks around $10e^-/s$ for an applied bias of 150 mV and a temperature of 28 K: we attribute this dark current to the "mux glow" discussed in Sec. 4.2, given its uniformity across the entire array and lack of bias dependence. The "mux glow" was also observed at temperatures of 30 and 32 K for this array, with a median "dark" current of 130 and $156e^-/s$, respectively, with a bias of 150 mV. This accounts for some of the loss of operability at 30 and 32 K c.f. 28 K. The percentage of operable pixels for different temperatures and applied biases are reported in Table 3, along with the well depth requirements. Median dark current and well depth measured for this array are shown in Table 4.

Figure 9 shows the discharge history of a pixel in the dark at three different applied biases for this device. The initial larger curvature observed in the signal with an initial applied bias of 350 mV is a consequence of quantum tunneling dark currents that are exponentially dependent on bias. As the pixel debiases, tunneling dark currents decrease and the dark current approaches the constant behavior with bias expected from steady "mux glow."

The major limiting factor in the operability of these arrays at larger bias and low temperatures has been tunneling dark currents, and it is much more evident at biases of 350 mV since trap-to-band and especially band-to-band tunneling are strongly dependent on the applied bias.[5,6,9] At higher applied bias, most of the pixels have dark currents exceeding $200e^-/s$, giving very low operabilities. The trap-to-band dark current is highly variable from pixel to pixel, but the band-to-band tunneling affects all of the pixels in the array.

The inoperability at low temperatures and low applied bias (~28 K and 150 mV, respectively) appears to be dominated by trap-to-band tunneling currents and not by band-to-band tunneling. This effect can be seen in the operability map for all four arrays (Fig. 10 for H1RG-18367) where a set of high dark current and/or low well depth, hence inoperable pixels form a cross-hatching pattern caused by the slight lattice mismatch between HgCdTe and the CdZnTe substrate. The lattice mismatch may cause the formation of misfit dislocations along the intersection of the {111} slip planes in zinc blende crystals and the growth plane of these arrays.[35–37] The fast Fourier transform (FFT) of

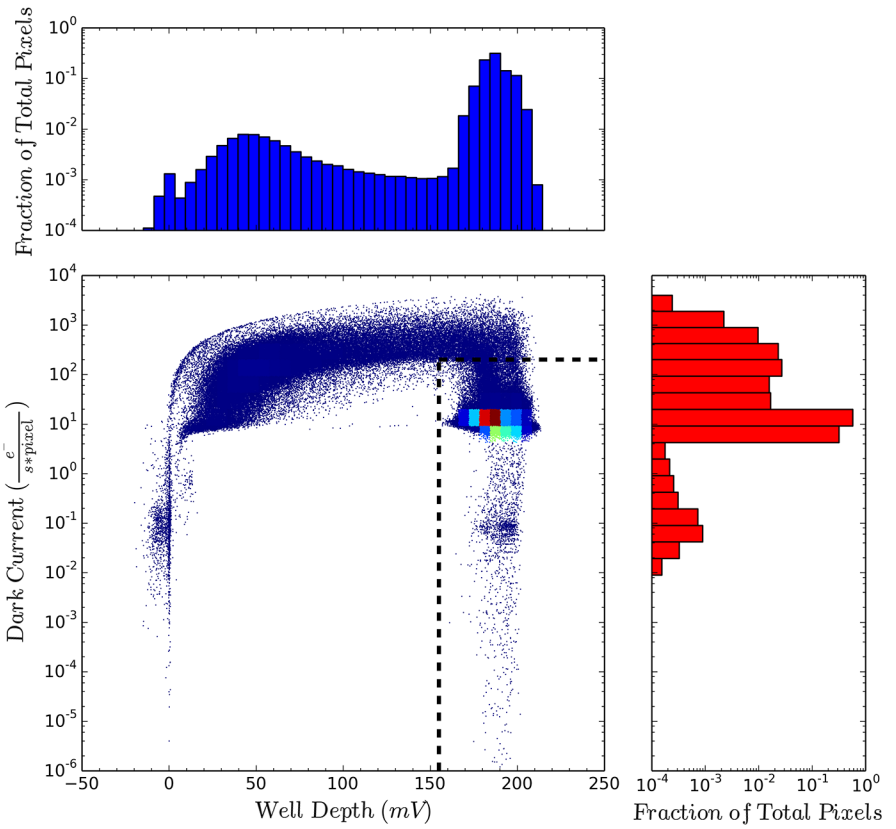

Fig. 8 Current in the dark versus well depth distribution per pixel for H1RG-18367 at a temperature of 28 K and an applied bias of 150 mV, showing operable pixels below and to the right of the dashed line. The well depth requirement of 155 mV (~41ke^-) was chosen to include the majority of the good pixels, and we kept this requirement for higher temperatures with the same applied bias. Note that the well depth corresponds to the actual initial detector bias, ranging from 155 to 225 mV at the beginning of the integration among the operable pixels for this data set.

Table 3 Operability pixel percentage for H1RG-18367 with different applied biases and temperatures. Operability requirements include currents in the dark[a] below 200e^-/s and well depths greater than those indicated in the table.

Applied bias	Well depth minimum	$T = 28$ K	$T = 30$ K	$T = 32$ K
		Operability (%)		
150 mV	155 mV (~41ke^-)	91.4	90.9	88.9
250 mV	255 mV (~59ke^-)	90.1	89.5	88.2
350 mV	310 mV (~67ke^-)	1.4	0.5	3.9

[a]A glow from the mux affected all of the dark current measurements for this array. This "mux glow" was highly variable, with median current of ~10, 130, and 156e^-/s at temperatures of 28, 30, and 32 K, respectively, with an applied bias of 150 mV.

Table 4 Median dark current and well depth for H1RG-18367. "Mux glow" was present in all dark current measurements. With 350 mV of bias, the decrease of dark current with increasing temperature (due to increasing the band gap energy) is indicative of tunneling dark currents.

Applied bias	$T = 28$ K	$T = 30$ K	$T = 32$ K
	Median dark current (e^-/s)		
	Median well depth (ke^-, mV)		
150 mV	10	130	156
	50, 186	50, 185	48, 180
250 mV	12	116	139
	67, 287	67, 286	66, 281
350 mV	379	359	321
	82, 379	82, 379	82, 376

the operability map on the upper left corner of Fig. 10 shows the cross-hatching lines distinctly but rotated by 90 deg.

The pattern consists of a set of three lines that have been identified by other authors[35,36] to lie parallel to the $[\bar{2}31]$, $[\bar{2}13]$, and $[01\bar{1}]$ directions. The angles between the three cross-hatching lines (shown in Fig. 11) were calculated by applying the Hough transform to the FFT image. The angles found in this work, $\alpha = 44.4$ deg and $\beta = 67.9$ deg, agree with the angles found in Refs. 35 and 36. Shapiro et al.[38] see the same pattern along the three cross-hatching directions as QE variation on subpixel scales on a 2.5-μm cutoff HgCdTe array, in addition to a cluster of high dark current pixels that lie along only one of the cross-hatching directions.

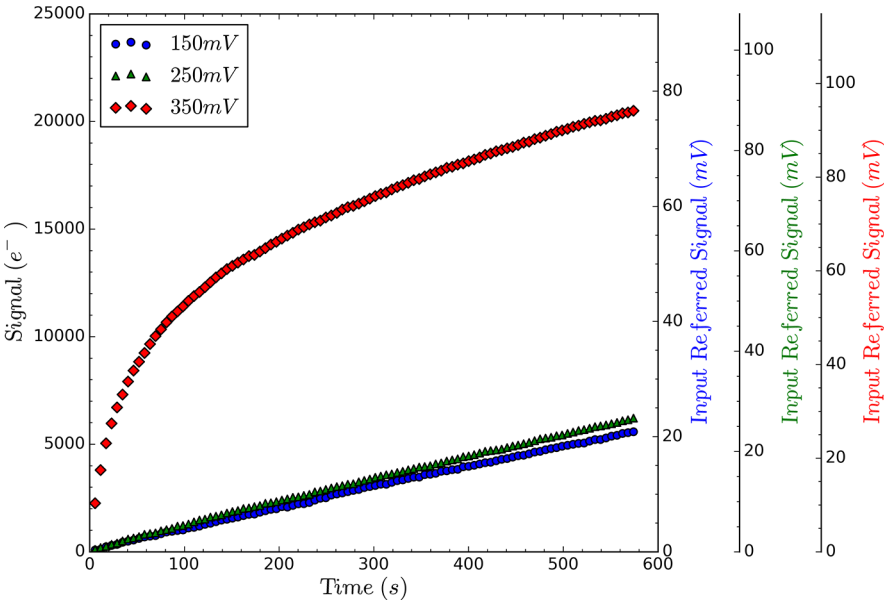

Fig. 9 Discharge history for pixel [532, 468] from H1RG-18367 at a temperature of 28 K and at applied reverse bias of 150, 250, and 350 mV in the dark. On the left *y*-axis scale, we show the signal in electrons, and the right *y*-scale axis shows the input referred signal in mV. The three different scales on the right correspond to the different diode capacitance measured (from left to right) at 150, 250, and 350 mV of applied biases. This pixel is inoperable at 350 mV of applied bias since the initial dark current exceeds the 200e^-/s cutoff.

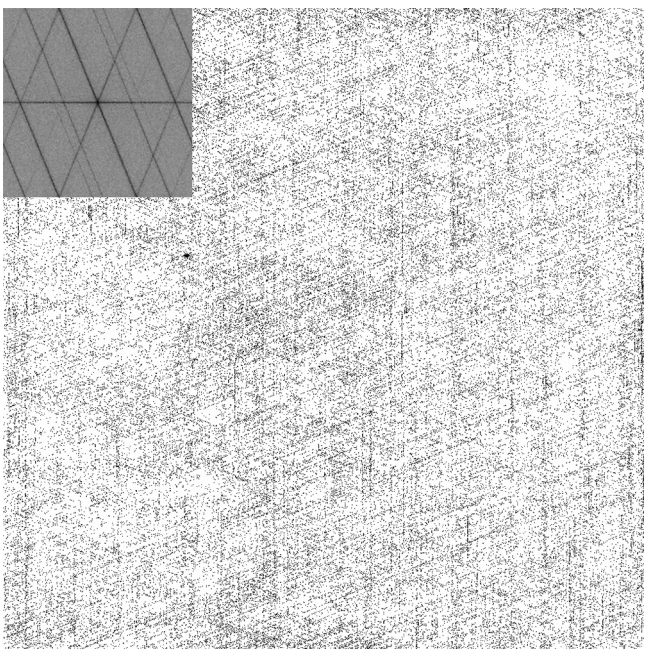

Fig. 10 Operability map for H1RG-18367 at a temperature of 28 K and applied bias of 150 mV, where inoperable pixels are shown in black. The (log magnitude) FFT of the operability map is shown in the upper-left corner.

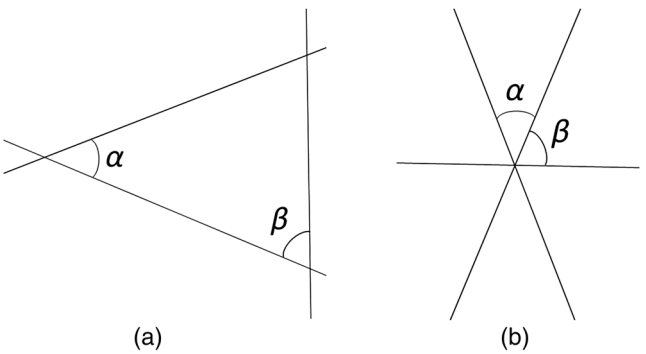

Fig. 11 Diagram of (a) the three cross-hatching lines that were observed in the operability map, and (b) in the (log magnitude) FFT of the operability map. The angles, $\alpha = 44.4$ deg and $\beta = 67.9$ deg, were determined by applying the Hough transform on the FFT image.

4.4.2 *H1RG-18508*

H1RG-18508 has a higher operability (Table 5) at higher temperatures than its counterpart H1RG-18367 (both were grown and processed in the same way, and both have similar cutoff wavelengths), and "mux glow" was not detected for this array. The dark current versus well depth distribution for this array at 28 K and an applied bias of 150 mV is shown in Fig. 12, where the majority of pixels had dark currents below $1e^-$/s. Median dark current and well depths are presented in Table 6.

The operabilities at 350 mV of applied bias are below 1% at all temperatures and have therefore been omitted from the operability table. The inoperability at larger applied bias is evidence of tunneling dark currents. The large curvature in the dark signal versus time curve is observed with increasing bias in Fig. 13, which is a hallmark of tunneling dark currents. The SUTR data obtained with an applied bias of 150 mV are linear as is expected if thermal dark currents (diffusion and G-R, which are a weak function of bias), a light leak, or a mux glow are dominating the dark current as the pixel debiases.

Table 5 Operability pixel percentage for H1RG-18508 with different applied biases and temperatures. Operability requirements include dark currents below 200e^-/s and well depths greater than those indicated in the table.

		$T = 28$ K	$T = 30$ K	$T = 32$ K	$T = 33$ K	$T = 34$ K	$T = 35$ K	$T = 36$ K
Applied bias	Well depth minimum	Operability (%)						
150 mV	155 mV (~41ke^-)	93.7	93.5	93.2	92.9	92.0	61.5	63.7
250 mV	245 mV (~58ke^-)	89.4	91.5	91.4	91.0	89.9	81.1	67.2

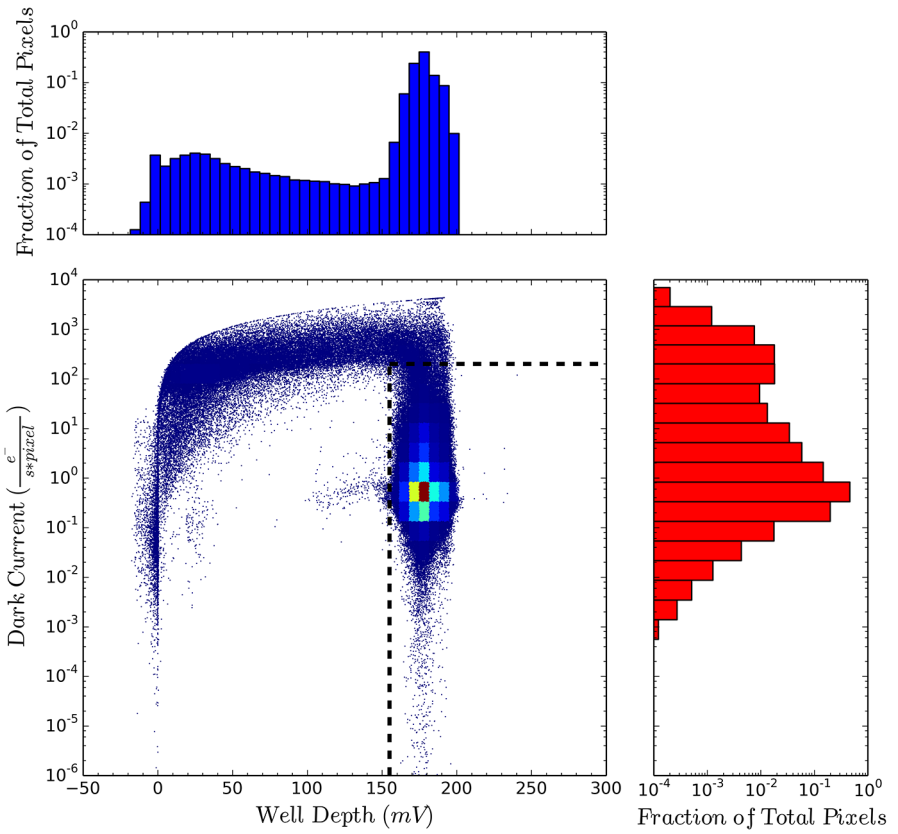

Fig. 12 Dark current versus well depth distribution per pixel for H1RG-18508 with an applied bias of 150 mV at a temperature of 28 K. Operable pixels lie below and to the right of the dashed line. The detector bias at the beginning of integration is similar to that of array H1RG-18367 (c.f. Fig. 8).

Table 6 Median dark current and well depth for H1RG-18508.

	$T = 28$ K	$T = 30$ K	$T = 32$ K	$T = 33$ K	$T = 34$ K	$T = 35$ K	$T = 36$ K
	Median dark current (e^-/s)						
Applied bias	Median well depth (ke^-, mV)						
150 mV	0.5	1.4	6	14	32	65	143
	46, 177	45, 173	45, 171	44, 170	44, 169	41, 157	42, 160
250 mV	57	39	34	39	51	71	144
	65, 275	64, 271	63, 269	63, 268	63, 267	60, 254	60, 253
350 mV	780	764	730	713	693	510	279
	73, 328	74, 331	76, 337	76, 341	77, 344	76, 341	74, 331

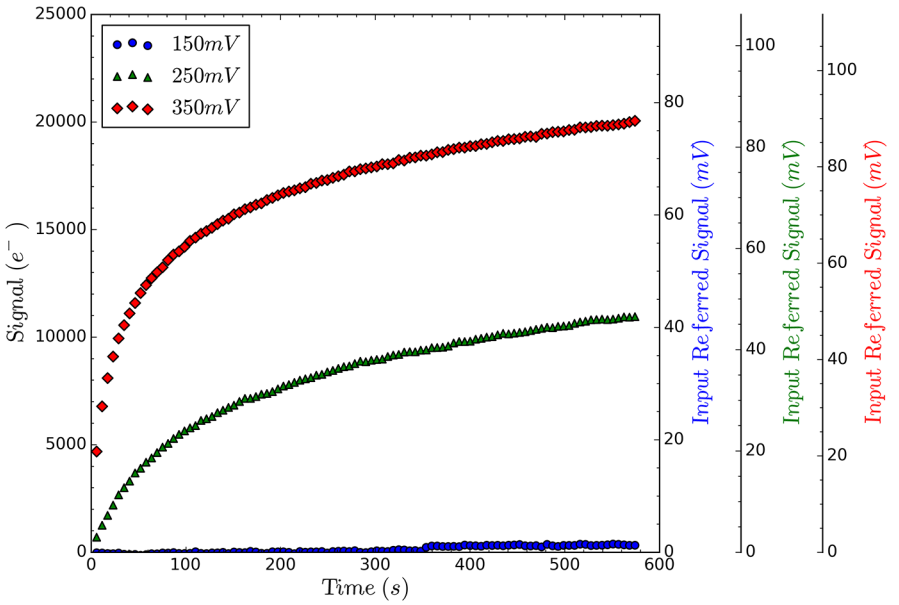

Fig. 13 Discharge history for pixel [543, 424] from H1RG-18508 at a temperature of 28 K in the dark. The initial dark currents (and well depths) for three SUTR curves at 150, 250, and 350 mV are: $0.4e^-$/s (181 mV), $120e^-$/s (281 mV), and $807e^-$/s (326 mV), respectively.

4.4.3 *H1RG-18369*

This array has a similar dark current and well depth distribution as H1RG-18508, where the majority of the pixels achieved dark current levels less than $1e^-$/s at a temperature of 28 K and an applied bias of 150 mV. Table 7 shows the operability for this array, where the unusual drop in operability when increasing the temperature by one degree with an applied bias of 150 and 250 mV is most likely due to "mux glow." Table 8 shows the median dark current and well depth for this array, where the increase in median dark current by a factor of ~100 at a temperature of 34 K and 150 mV of bias cannot be explained by any of the known dark current mechanisms. In addition, the decrease in dark current with increasing temperature, for an applied bias of 350 mV from 28 to 32 K, is consistent with tunneling dark currents. If the increase in dark current at 33 K was due to thermal currents overtaking tunneling currents, we would expect the dark current to continue to rise with increasing temperature, and this is not the case. Figure 14 shows the dark current distribution for this array at 33 and 34 K with an applied bias of 150 mV.

Furthermore, despite the experimental design used to reduce tunneling dark currents, this array also exhibited low operabilities at 350 mV (<1%) as did the standard growth arrays (H1RG-18367 and 18508).

4.4.4 *H1RG-18509*

To mitigate the effects of the tunneling dark currents, Teledyne developed several modifications to its baseline NEOCam design, designated as designs 1 and 2, shown in Table 1. H1RG-18509 was from the design-2 lot split and outperformed the other LW13 arrays in terms of operability at all applied biases but especially at 350 mV and at higher temperatures (Table 9). Table 10 shows the median dark current and well depths measured for this array at different temperatures and applied bias. This array has a slightly shorter wavelength cutoff compared with the standard growth arrays.

Design 2 had a positive effect on reducing the quantum tunneling currents as is readily apparent in curves of the time dependence of charge collected in the dark, where most of the individual SUTR curves for H1RG-18509 did not exhibit highly curved discharge behavior such as observed for the other arrays. Figure 15 shows the histogram of curvature values (initial second derivative of the SUTR curves) per pixel, for all LW13

Table 7 Operability pixel percentage for H1RG-18369 with different applied biases and temperatures. Operability requirements include dark currents below $200e^-$/s and well depths greater than those indicated in the table.

		$T = 28$ K	$T = 30$ K	$T = 32$ K	$T = 33$ K	$T = 34$ K	$T = 35$ K
Applied bias	Well depth minimum	Operability (%)					
150 mV	155 mV (~$37ke^-$)	93.0	92.8	92.7	92.6	0.0[a]	0.0[a]
250 mV	255 mV (~$57ke^-$)	91.5	91.3	91.1	0.0[a]	0.0[a]	0.0[a]

[a]The "mux glow" affected the noted operabilities for this array, increasing the median dark current by a factor of ~100 when the temperature was increased from 33 to 34 K with an applied bias of 150 mV, and by a factor of ~43 when increasing the temperature from 32 to 33 K with an applied bias of 250 mV, effectively making the entire array inoperable.

Table 8 Median dark current and well depth for H1RG-18369.

	$T = 28$ K	$T = 30$ K	$T = 32$ K	$T = 33$ K	$T = 34$ K	$T = 35$ K
	Median dark current (e^-/s)					
Applied bias	Median well depth (ke^-, mV)					
150 mV	0.5	0.7	2.4	5	481[a]	698[a]
	43, 182	42, 177	41, 174	43, 181	41, 173	40, 169
250 mV	24	17	14	604[a]	600[a]	791[a]
	64, 283	63, 278	62, 275	62, 275	62, 273	61, 269
350 mV	730	682	616	989[a]	930[a]	957[a]
	78, 355	78, 357	79, 359	80, 364	80, 364	79, 361

[a]Dark currents affected by a "mux glow."

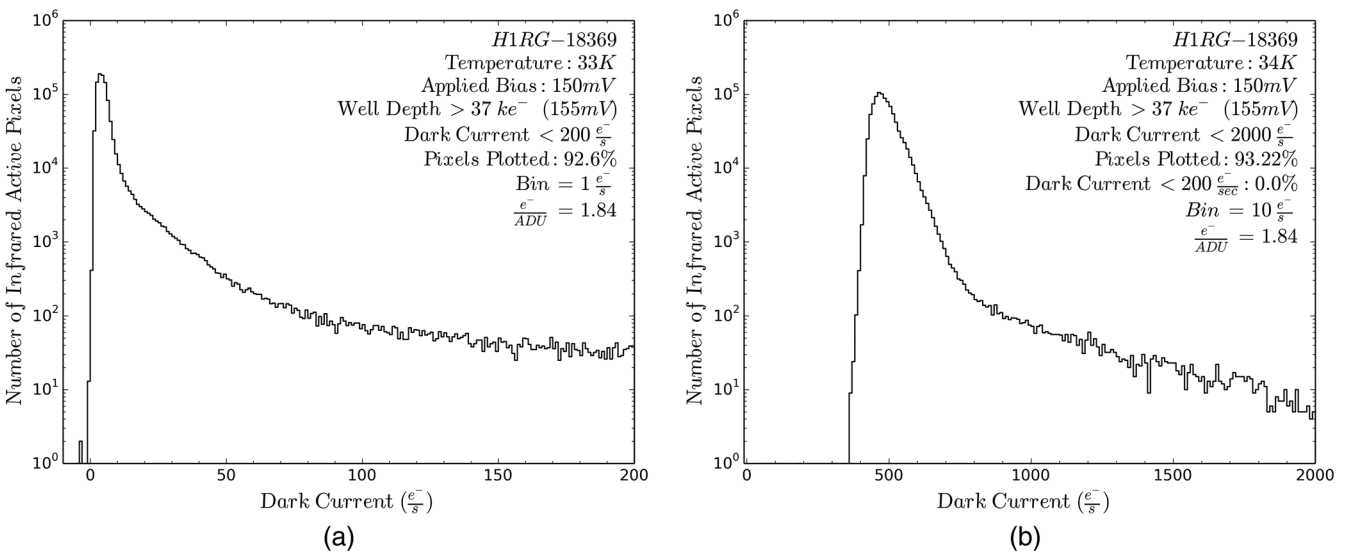

Fig. 14 Dark current distribution for pixels with well depths greater than 37 ke^- at temperatures of (a) 33 K and (b) 34 K, both with an applied bias of 150 mV. The increase in current by a factor of ~100 by increasing the temperature by 1 K is most probably due to "mux glow."

Table 9 Operable pixel percentage for H1RG-18509 with different applied biases and temperatures. Operability requirements include dark currents below 200e^-/s and well depths greater than those indicated in the table.

		$T = 28$ K	$T = 30$ K	$T = 32$ K	$T = 34$ K	$T = 35$ K	$T = 36$ K
Applied bias	Well depth minimum	Operability (%)					
150 mV	155 mV (~38ke^-)	95.9	95.9	95.8	95.7	94.7	85.5
250 mV	255 mV (~59ke^-)	94.7	94.6	94.5	94.0	92.7	44.7
350 mV	355 mV (~75ke^-)	90.3	92.2	93.1	92.3	90.8	19.4

arrays with an applied bias of 350 mV. The peak of the histogram near zero for H1RG-18509 demonstrates a nearly linear behavior in the charge collected over time for the majority of pixels, in contrast to the behavior of the other three arrays shown by the peaks of their respective histograms shifted toward larger negative values. At these higher biases, band-to-band tunneling current becomes dominant and this affects all pixels.

5 Dark Current Model Fits

The effects of tunneling dark currents were shown in Secs. 4.4.1–4.4.4, and comparing our measurements to theory will allow us to assess the degree to which each of the tunneling components is dominant and how we can mitigate these effects further as we continue to extend the cutoff wavelength for the second phase of this project.

Table 10 Median dark current and well depth for H1RG-18509.

	$T = 28$ K	$T = 30$ K	$T = 32$ K	$T = 34$ K	$T = 35$ K	$T = 36$ K
	Median dark current (e^-/s)					
Applied bias	Median well depth (ke^-, mV)					
150 mV	0.2	0.7	3.5	19	41	82
	44, 182	43, 177	43, 174	42, 174	42, 173	40, 163
250 mV	0.3	0.8	3.8	20	43	76
	65, 283	64, 278	63, 276	63, 275	63, 274	59, 255
350 mV	1.8	1.8	4	19	42	67
	81, 385	80, 380	80, 378	80, 377	80, 376	74, 348

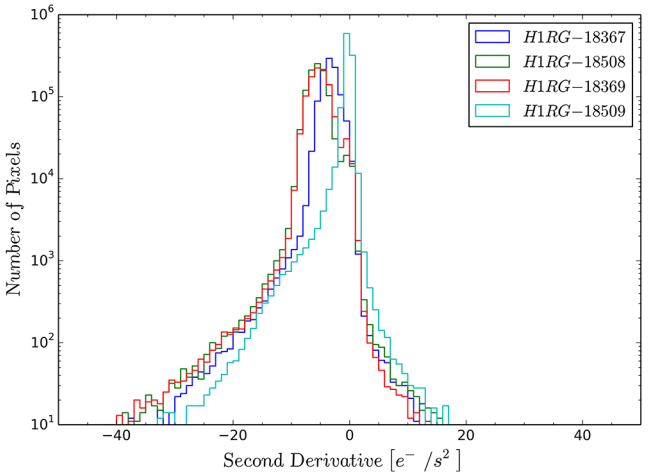

Fig. 15 Histogram of the initial curvature from SUTR curves for all LW13 arrays at 28 K and an applied bias of 350 mV.

Given the different dependences on temperature and bias for the dark current mechanisms, we fit the thermal currents, which are strongly temperature dependent, to dark current versus temperature (*I-T*) data, and the tunneling currents are fit to dark current versus bias (*I-V*) data given their strong dependence on bias.

5.1 *Dark Current Versus Temperature*

I-T data consist of two different data sets: (1) the initial dark current per pixel, which was obtained at the stable temperatures reported in the operability tables in Secs. 4.4.1–4.4.4, and (2) the warm-up data taken when the liquid helium in our dewar runs out. Four full array frames are read after resetting the array in SUTR mode, immediately followed by an array reset and reading four subarray (32 rows, all columns) frames in SUTR mode. This data-taking process continued until the temperature reached 77 K. The dark current was then obtained by subtracting the pedestal from the following three frames, taking the average signal from the pedestal subtracted frames and dividing by the average integration time.

The integration time between the full array data frames is 5.8 s and 0.2 s for the subarray frames. At lower temperatures, the amount of charge collected by pixels in 0.2 s is on the order of the read-noise ($\sim 23e^-$); we therefore use the 5.8-s integration time data to form the *I-T* curve at these lower temperatures. As the temperature increases, so does the dark current, saturating the full array frames at a temperature of ~40 K. At a point before the full frames saturate, we used the subarray frames, which saturate at a higher temperature (~50 K), because of the shorter integration time.

5.2 *Dark Current Versus Bias*

SUTR data sets taken to measure the dark current and well depth are used to obtain *I-V* curves. The dark current is obtained by taking the difference between sequential data points along the dark signal versus time curve and dividing by the time interval between those points, whereas the actual bias across the diode is calculated by subtracting the input-referred signal from the well depth level (see the upper curves in Figs. 9 and 13). Only partial *I-V* curves can be obtained from the dark SUTR curves since we do not completely debias the devices in the dark. To reduce the effect of thermal dark currents on the *I-V* curve, tunneling dark currents are fit to the lowest temperature *I-V* curve (28 K).

The *I-V* curve for the 150-mV SUTR set is not used since the data for reasonably good pixels typically span less than 5 mV of bias. Instead, only the initial dark current and well depth are used as the lowest bias data point. The same is done for H1RG-18509 for the three applied biases since most pixels discharge less than 5 mV in the dark signal versus time data.

5.3 *Fitting Process and Caveats*

Equations (9) and (11) in Sec. 2.3 show that tunneling currents are exponentially dependent on band gap and electric field in the junction region. The *I-V* curves of several operable pixels at large applied bias (>200 mV) matched the trend of a fit to band-to-band tunneling, where the only parameter to fit is $E_g^{3/2}/E \equiv \beta$. If indeed these pixels (or the majority) are dominated by band-to-band tunneling, this would allow us to get the most accurate estimate of the parameter β since other dark current mechanisms have several other parameters to fit, which can lead to a nonunique set of fitted parameters. Figure 16(a) shows an example of an operable pixel in H1RG-18508. Inoperable pixels required the addition of trap-to-band tunneling to fit the *I-V* data. Figure 16(b) shows an inoperable pixel in H1RG-18508, where the β parameter of the operable nearest neighbor pixels used to fit band-to-band tunneling current is shown to be orders of magnitude below the measured dark current and hardly contributes to the fit.

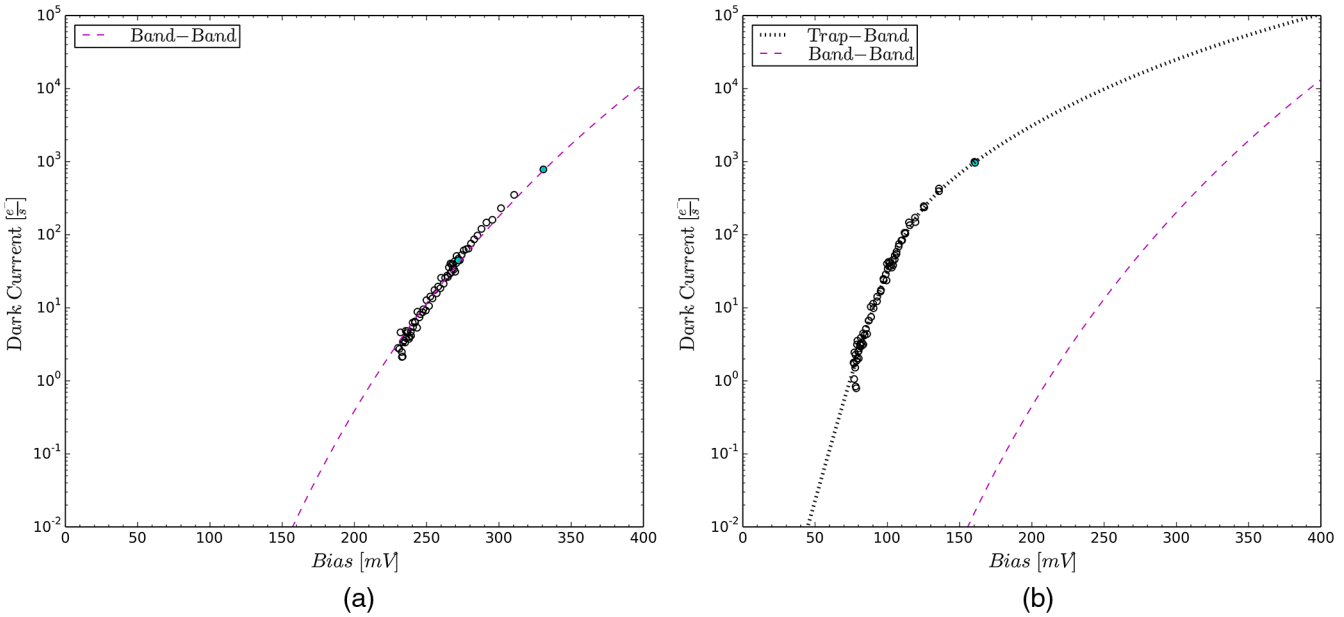

Fig. 16 Dark current versus bias at a temperature of 28 K for (a) an operable and (b) inoperable (at 150 mV of applied bias) pixel in H1RG-18508.

Unlike band-to-band tunneling where β is the only unknown parameter, trap-to-band tunneling requires the fitting of five additional parameters (see Sec. 2.3). Furthermore, the fitted trap-to-band tunneling heavily depends on the parameters' initial guess, which may not be unique.

Therefore, only band-to-band is initially fitted to the larger applied bias *I-V* data of operable pixels to estimate the value of β. The following step to model the dark current was to then fit the thermal dark currents (diffusion and G-R) to the higher temperature *I-T* data. Finally, the test dewar light leak or "mux glow" is fitted, along with trap-to-band tunneling if necessary.

When estimating the value of β in H1RG-18367 and H1RG-18509, an additional constant current was added to the *I-V* data along with band-to-band tunneling (similar to that shown in Fig. 19 on individual pixels) because the large bias data were not completely dominated by band-to-band tunneling. In the case of H1RG-18367, the "glow" from the multiplexer

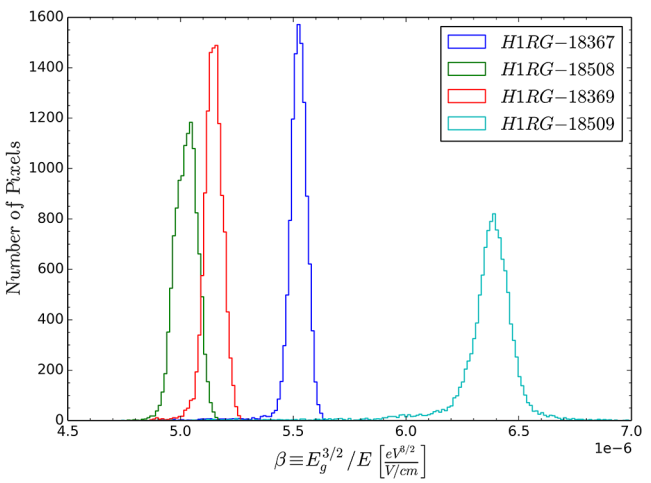

Fig. 17 Fitted β value distribution, with an actual reverse bias of 300 mV, to operable pixels in the central 32 rows (for which we have warm-up data) and 400 columns of the array.

(discussed in Secs. 4.2 and 4.4.1) has a considerable effect on the *I-V* data up to 300 mV of bias, whereas H1RG-18509 is dominated by a possible $<1e^-/s$ light leak in the test dewar and G-R up to a bias of ~350 mV. Since G-R current does not have a large bias dependence in the range of interest, the light leak plus the G-R current in H1RG-18509 were modeled as a constant current when estimating β.

Figure 17 shows the distribution of fitted β values to a 32 × 400 pixel region in the four arrays presented here.

5.4 *Dark Current Model Results*

Figure 18 shows the dark current Arrhenius plot at a detector bias of 276 mV and dark current versus bias (at a temperature of 28 K) for 36 operable pixels in H1RG-18508. The *I-T* data shown are the average of all 36 pixels, where the error bars on the filled circles correspond to the standard deviation of the mean in the dark current values for the averaged pixels. The individual *I-V* data curves for each of the 36 pixels are displayed along with the mean initial dark current and actual bias (filled circles) for the 36 pixels corresponding to 150, 250, and 350 mV of applied bias. The shaded region's upper and lower bounds coincide with the band-to-band tunneling calculated from the β values that are two standard deviations away from the mean of the fitted β value distribution in Fig. 17, and the single band-to-band tunneling curve is calculated from the mean β value of the 36 pixels.

The *I-V* data for the 36 pixels in Fig. 18(b) follow the trend of band-to-band tunneling with slightly different β values at biases >200 mV. The dark current models fitted to the *I-T* data shows that, up to a temperature of ~32 K, the dark current of operable pixels is dominated by band-to-band tunneling. At higher temperatures G-R and diffusion currents are the dominating components.

Similar to H1RG-18508, the majority of the pixels in the other three arrays (Figs. 19–21) that were operable at a temperature of 28 K and 250 mV of applied bias were dominated by band-to-band tunneling at larger biases

The observed "mux glow" in H1RG-18367 is large enough to dominate the dark current up to a bias of ~300 mV (see

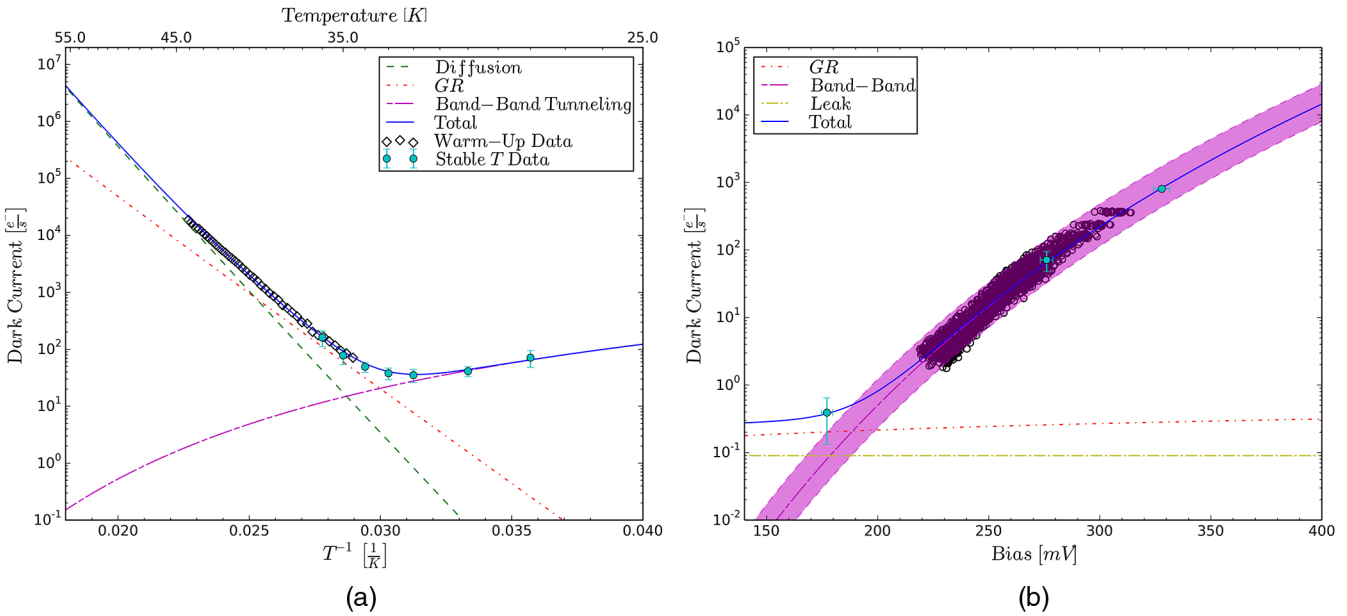

Fig. 18 (a) Dark current versus temperature (mean actual back-bias of 276 mV) averaged data of 36 operable pixels in H1RG-18508. The error bars correspond to $\pm$ one standard deviation of the mean in the dark current values for the averaged pixels. (b) Individual dark current versus bias (at 28 K) data curves (empty circle data points) for the same 36 pixels shown in (a). The solid cyan circle data points are the average of the initial dark current and actual bias for the 36 pixels. The shaded region in (b) corresponds to the band-to-band tunneling calculated from the β value $\pm$ two standard deviations from the mean, and the single band-to-band tunneling curve corresponds to that of the mean β value of the 36 pixels.

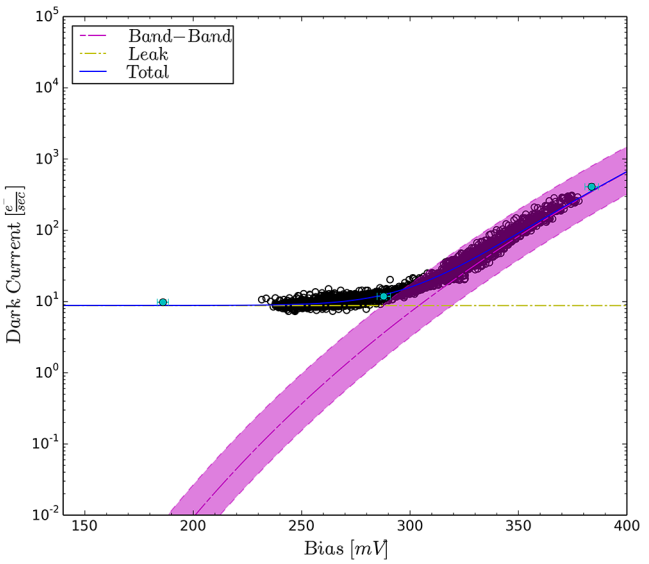

Fig. 19 Dark current versus bias data curves for 36 pixels that were operable at a temperature of 28 K and applied bias of 250 mV in H1RG-18367 at a temperature of 28 K. The constant leak current that was fitted corresponds to the "mux glow."

Fig. 19), and in the linear behavior of the SUTR curve for the pixel in Fig. 9. Thermal dark currents were not fitted to this array as warm-up data are not available.

The warm-up data for H1RG-18369 were obtained with an applied bias of 150 mV, where the *I-T* data in Fig. 20(a) show that at 28 K, the dark current is limited by a possible $0.3e^-/s$ light leak in the test dewar. The 34 and 35 K stable data points, which were affected by the "mux glow," do not follow the behavior expected from any of the dark current mechanisms, further confirming that the anomalous increase of dark current from 33 to 34 K is not due to thermal currents. The "mux glow" was not present in the warm-up data.

The increased tunneling currents in these devices, compared with the LW10 devices, were expected given the smaller bandgap. H1RG-18509 was designed to address this concern. A substantial decrease in band-to-band tunneling current in this array compared with the other three arrays can be seen in Fig. 21. The small curvature in the SUTR curves (shown in the double derivative at the beginning of the SUTR curves in Fig. 15) for the majority of the pixels for this array is due to the relatively small tunneling current found in the *I-V* data [Fig. 21(b)]. As a consequence, we are able to achieve larger well depths by applying a large bias ($\sim 75ke^-$ with an applied bias of 350 mV). The warm-up data for this array were taken with an applied bias of 250 mV. Dark current data for this array above 29 K are dominated by G-R and diffusion, whereas lower temperature dark current, which is well below $1e^-/s$, approaches the light leak level.

The apparent dominance of band-to-band tunneling at higher biases in operable pixels for all arrays is very encouraging, as further enhancements in Teledyne's design to increase β will decrease this tunneling component in future longer wavelength devices.

6 Discussion on Linear Dark Current Regimes

We have shown that tunneling dark currents dominate the operabiilty of these devices, where the nonlinear effects of these currents may present a problem in the calibration of low signal data.

The reduction of tunneling dark currents in H1RG-18509 allows for a linear dark current calibration at low signals since the dark current versus time is nearly linear at biases as large as

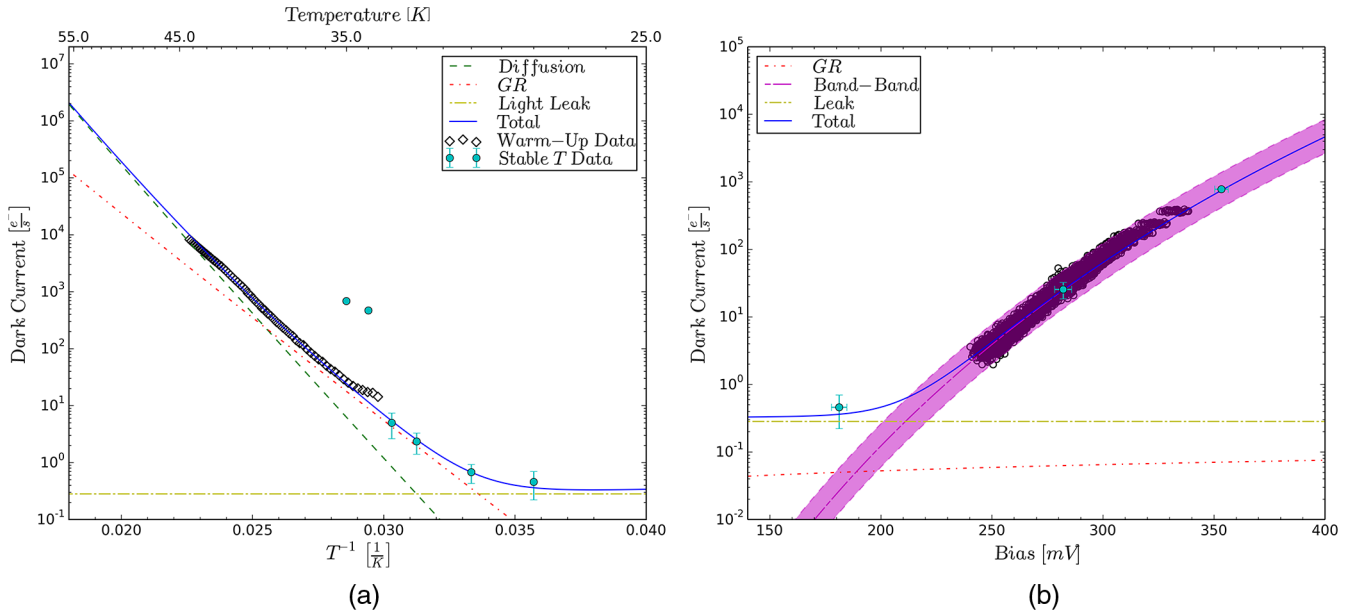

Fig. 20 (a) Dark current versus temperature (applied bias of 150 mV) averaged data of 36 operable pixels in H1RG-18369. The mean actual bias of 181 mV, corresponding to the 28 K stable data point, was used to fit the dark current models. (b) Individual dark current versus bias (at 28 K) data curves for the same 36 pixels shown in (a). The 33 and 34 K stable temperature data points in (a) were affected by a "mux glow," increasing the dark current above the expected value from thermal dark currents.

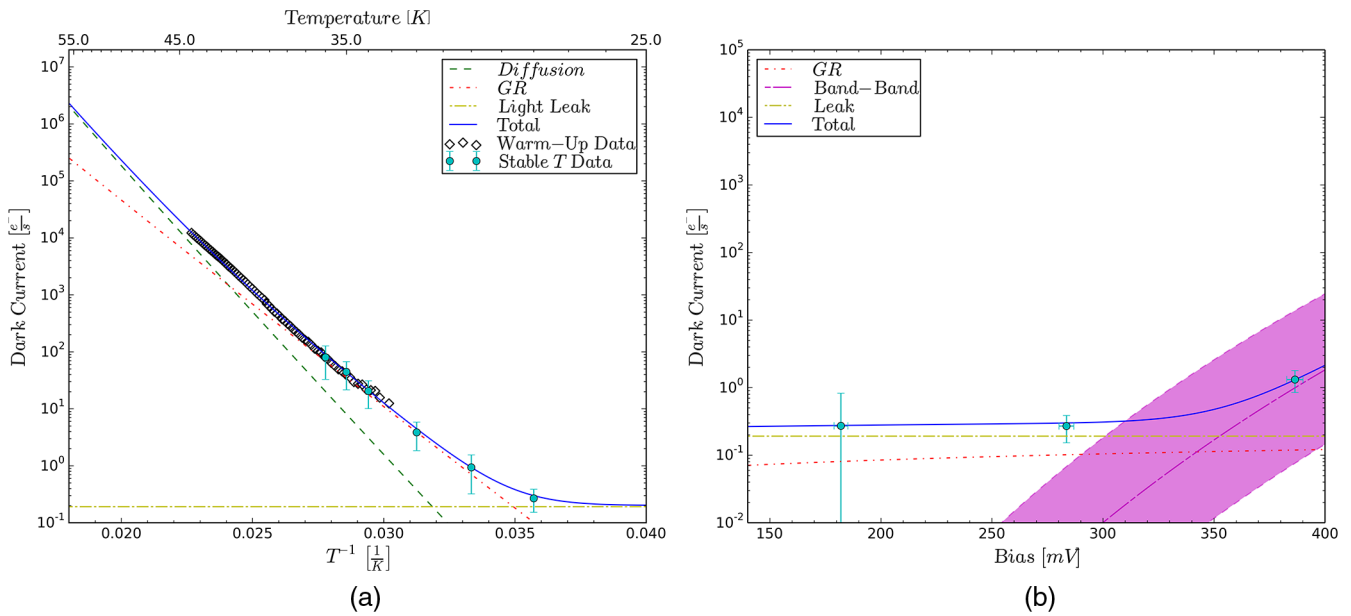

Fig. 21 (a) Dark current versus temperature (applied bias of 250 mV) and (b) dark current versus bias (at 28 K) averaged data of 50 operable pixels in H1RG-18509. In (a), the mean actual bias of 284 mV, corresponding to the 28 K stable data point, was used to fit the dark current models.

350 mV. The nonlinear effects on collected signal versus time due to large band-to-band tunneling currents seen in the other three arrays at large biases may be modeled for each of the operable pixels in an attempt to calibrate it, but the exact (or very close to) initial actual bias across each pixel is needed since the tunneling currents vary appreciably as pixels debias.

Alternatively, the three arrays that show large band-to-band currents can be operated in regimes where the dark current is not dominated by band-to-band tunneling.

In the low applied bias regime where band-to-band tunneling is negligible, thermal dark currents would be the dominant source of dark current and could be calibrated at stable temperatures since these currents are approximately linear (above ~25 mV of reverse bias) as pixels debias. For applications that require larger well depths than can be attained with the Hawaii-XRG multiplexers at the biases needed to operate in this regime ($\sim < 200$ mV), a capacitive transimpedance amplifier (CTIA) multiplexer could be used in its place. A CTIA multiplexer would allow the operation of these arrays at a constant voltage while signal is integrated, therefore, maintaining a constant dark current and with a much larger well depth at the expense of higher power dissipation and read noise.

Another solution to avoid nonlinear dark currents as a function of bias is to increase the operating temperature. Tunneling currents decrease with increasing temperature since the bandgap energy increases. At higher temperatures, the dark current due to thermal currents may be comparable to those from band-to-band tunneling at lower temperatures. Figure 18(a) shows that with an applied bias of 250 mV, the dark current in H1RG-18508 at 35 K is dominated by G-R and is comparable to that at 28 K, which is dominated by band-to-band tunneling.

7 Summary

We demonstrate the promising performance of four 13-μm cutoff wavelength arrays that all have high QE, low read noise, and operabilities close to or greater than 90% for temperatures of up to 32 K for an applied bias of 250 mV. At lower temperatures, the majority of pixels have dark currents below $1e^-/s$ for three of the four tested arrays while the fourth has currents of $\sim 10e^-/s$ due to a probable glow from the mux.

The cross-hatching pattern associated with the intersection of slip planes and the growth plane in HgCdTe detector arrays was observed for all four LW13 arrays in pixels with high dark currents and/or low well depths due to trap-to-band tunneling dark current. Cross-hatch patterns are generally related to the formation of misfits, generated either during growth or fabrication; further optimization of the process could potentially result in further improvements. Pixels that were operable at a temperature of 28 K and 250 mV of applied bias (~90% for all four arrays) appear to be dominated by band-to-band tunneling dark current at biases greater than about 200 mV for three of the four arrays. Band-to-band tunneling is also responsible for the inoperability of these three arrays with an applied bias of 350 mV. H1RG-18509 was shown to have an improved performance at larger applied biases with the mitigation of the band-to-band tunneling presumably because of Teledyne's experimental structure and better operability at lower bias, due to less trap-to-band tunneling. At a temperature of 28 K and an applied reverse bias of 350 mV, the median dark current and well depth for this array is $1.8e^-/s$ and $81ke^-$, respectively.

These long-wave arrays that can be passively cooled in space will provide cost-savings, offer a longer operational time-frame, and entail no decrease in sensitivity-thereby improving remote sensing capabilities and performance for future space missions.

TIS has completed the growth of several 15 μm cutoff wavelength arrays, and results on those arrays will be reported separately once characterization tests and analysis are complete.

Acknowledgments

The University of Rochester group acknowledges support by NASA Grant No. NNX14AD32G S07. M. Cabrera acknowledges the NASA grant, New York Space grant, and the Graduate Assistance in Areas of National Need (GAANN) grant for partially supporting his graduate work. The authors also thank the referees for their feedback and constructive comments to improve the paper.

References

1. M. W. Werner et al., "The Spitzer space telescope mission," *Astrophys. J. Suppl. Ser.* **154**(1), 1–9 (2004).
2. R. D. Gehrz et al., "The NASA Spitzer space telescope," *Rev. Sci. Instrum.* **78**(1), 011302 (2007).
3. A. Mainzer et al., "Characterization of flight detector arrays for the wide-field infrared survey explorer," *Proc. SPIE* **7021**, 70210X (2008).
4. G. L. Hansen and J. L. Schmit, "Calculation of intrinsic carrier concentration in $Hg_{1-x}Cd_xTe$," *J. Appl. Phys.* **54**(3), 1639–1640 (1983).
5. J. Wu, "Development of infrared detectors for space astronomy," PhD Thesis, University of Rochester (1997).
6. R. B. Bailey et al., "Prospects for large-format IR astronomy FPAs using MBE-grown HgCdTe detectors with cutoff wavelength >4 μm," *Proc. SPIE* **3354**, 77–86 (1998).
7. C. M. Bacon et al., "Further characterization of Rockwell Scientific LWIR HgCdTe detector arrays," *Proc. SPIE* **5563**, 11 (2004).
8. C. M. Bacon, "Development of long wave infrared detectors for space astronomy," PhD Thesis, University of Rochester (2006).
9. C. M. Bacon et al., "Effect of dislocations on dark current in LWIR HgCdTe photodiodes," *Proc. SPIE* **7742**, 77421U (2010).
10. M. Carmody et al., "Threading and misfit-dislocation motion in molecular-beam epitaxy-grown HgCdTe epilayers," *J. Electron. Mater.* **32**(7), 710–716 (2003).
11. E. C. Smith et al., "JWST near infrared detectors: latest test results," *Proc. SPIE* **7419**, 741907 (2009).
12. M. L. Dorn et al., "Proton irradiation results for long-wave HgCdTe infrared detector arrays for Near-Earth Object Camera," *J. Astron. Telesc. Instrum. Syst.* **2**(3), 036002 (2016).
13. C. W. McMurtry et al., "Candidate 10 micron HgCdTe arrays for the NEOCam Space Mission," *Proc. SPIE* **9915**, 99150D (2016).
14. M. Dorn et al., "A monolithic 2k x 2k LWIR HgCdTe detector array for passively cooled space missions," *Proc. SPIE* **10709**, 1070907 (2018).
15. M. Kinch, "Chapter 7 metal-insulator-semiconductor infrared detectors," Mercury Cadmium Telluride, R. Willardson, and A. C. Beer, Eds., *Semicond. Semimetals* **18**, 313–378 (1981).
16. S. M. Sze, *Physics of Semiconductor Devices*, John Wiley & Sons, New York (1981).
17. M. A. Kinch, *State-of-the-Art Infrared Detector Technology*, SPIE Press, Bellingham, Washington (2014).
18. J. T. Montroy et al., "Advanced imaging sensors at Rockwell Scientific Company," *Proc. SPIE* **4721**, 1–15 (2002).
19. M. Loose et al., "HAWAII-2RG: a 2k x 2k CMOS multiplexer for low- and high-background astronomy applications," *Proc. SPIE* **4850**, 1–13 (2003).
20. M. Loose et al., "High-performance focal plane arrays based on the HAWAII-2RG/4RG and the SIDECAR ASIC," *Proc. SPIE* **6690**, 66900C (2007).
21. M. Reine, A. Sood, and T. Tredwell, "Chapter 6 photovoltaic infrared detectors," Mercury Cadmium Telluride, R. Willardson, and A. C. Beer, Eds., *Semicond. Semimetals* **18**, 201–311 (1981).
22. C. T. Sah, R. N. Noyce, and W. Shockley, "Carrier generation and recombination in P-N junctions and P-N junction characteristics," *Proc. IRE* **45**(9), 1228–1243 (1957).
23. P. Neudeck, W. Huang, and M. Dudley, "Breakdown degradation associated with elementary screw dislocations in 4H-SiC P^+N junction rectifiers," *Solid-State Electron.* **42**(12), 2157–2164 (1998).
24. P. G. Neudeck, W. Huang, and M. Dudley, "Study of bulk and elementary screw dislocation assisted reverse breakdown in low-voltage (<250 V) 4H-SiC p^+n junction diodes. I: DC properties," *IEEE Trans. Electron Devices* **46**(3), 478–484 (1999).
25. K. V. Ravi, C. J. Varker, and C. E. Volk, "Electrically active stacking faults in silicon," *J. Electrochem. Soc.* **120**(4), 533–541 (1973).
26. J. D. Benson et al., "Characterization of dislocations in (112)B HgCdTe/CdTe/Si," *J. Electron. Mater.* **39**, 1080–1086 (2010).
27. A. C. Moore et al., "Operation and test of hybridized silicon p-i-n arrays using open-source array control hardware and software," *Proc. SPIE* **5017**, 1–14 (2003).
28. A. M. Fowler and I. Gatley, "Demonstration of an algorithm for read-noise reduction in infrared arrays," *Astrophys. J. Lett.* **353**, L33 (1990).
29. J. D. Garnett and W. J. Forrest, "Multiply sampled read-limited and background-limited noise performance," *Proc. SPIE* **1946**, 395–404 (1993).
30. B. J. Rauscher et al., "Detectors for the James Webb space telescope near-infrared spectrograph. I. readout mode, noise model, and calibration considerations," *Publ. Astron. Soc. Pac.* **119**(857), 768–786 (2007).

31. L. Mortara and A. Fowler, "Evaluations of charge-coupled device (CCD) performance for astronomical use," *Proc. SPIE* **0290**, 6–15 (1981).
32. A. C. Moore, Z. Ninkov, and W. J. Forrest, "Interpixel capacitance in non-destructive focal plane arrays," *Proc. SPIE* **5167**, 204–215 (2004).
33. J. Wu et al., "Development of infrared focal plane arrays for space," *Rev. Sci. Instrum.* **68**(9), 3566–3578 (1997).
34. B. J. Rauscher et al., "Principal components analysis of a JWST NIRSpec detector subsystem," *Proc. SPIE* **8860**, 886005 (2013).
35. M. Martinka et al., "Characterization of cross-hatch morphology of MBE (211) HgCdTe," *J. Electron. Mater.* **30**, 632–636 (2001).
36. Y. Chang et al., "Surface morphology and defect formation mechanisms for HgCdTe (211)B grown by molecular beam epitaxy," *J. Electron. Mater.* **37**, 1171–1183 (2008).
37. J. Ayers, *Heteroepitaxy of Semiconductors: Theory, Growth, and Characterization*, CRC Press, Boca Raton, Florida (2007).
38. C. Shapiro, E. Huff, and R. Smith, "Intra-pixel response characterization of a HgCdTe near infrared detector with a pronounced crosshatch pattern," *Proc. SPIE* **10709**, 1070936 (2018).

Biographies of the authors are not available.